Real-space formulation of the mixed-basis pseudopotential method: Bulk structural properties of elemental copper

M. H. Kang, R. C. Tatar, E. J. Mele, and Paul Soven
Department of Physics and The Laboratory for Research on the Structure of Matter, University of Pennsylvania, Philadelphia, Pennsylvania 19104
(Received 7 July 1986)

We present a formulation of the mixed-basis expansion for electronic structure calculations, which allows calculations on systems in which there is a strongly localized component of the valence charge density. As in the conventional mixed-basis expansion, a small plane-wave basis is augmented with a set of auxiliary functions to describe the localized component of the wave functions. Unlike the conventional mixed-basis scheme, however, a fixed set of optimized *nonoverlapping* auxiliary functions are employed, so that matrix elements involving this set are calculable by very fast and accurate one-dimensional **k**-independent quadrature. The method is applied to study the electronic structure and bulk structural properties of Cu. The electronic structure, based on the pseudopotential of Bachelet, Hamann, and Schlüter, compares well with that obtained from other self-consistent state-of-the-art all-electron methods. The total energies for Cu in the fcc and bcc crystal structures are calculated and compared. We find that the fcc structure is favored at all densities, although the bcc exhibits an unusually stable high-density structure. A number of technical points relating to the use of these optimized local basis functions in band-structure calculations are discussed.

I. INTRODUCTION

Over the last several years pseudopotential theory has been shown to provide a powerful approach for studying the structural properties of solids.[1] Calculations based on the local-density approximation for the exchange and correlation energies of an interacting electron gas,[2–4] employing a class of "first-principles" pseudopotentials,[5] have correctly identified the stable high-symmetry crystal structures of a number of elements,[1] and in some cases have been used to predict the critical pressure[6,7] or temperature[8] of phase transitions between ordered high-symmetry phases.

It has been recognized for some time that the application of the pseudopotential method to either light elements or transition metals must be undertaken with some care. In both classes of systems the valence pseudopotential is quite strong in at least one angular momentum channel, so that a conventional plane-wave expansion in the solid state is of limited usefulness. Various computational schemes have been developed to circumvent this difficulty. For example, an expansion of the valence wave functions in Gaussian orbitals[9–11] has been used to study the electronic structure of carbon (which has a strong p pseudopotential) and of several transition elements, in which the d potential is very strong.

Alternatively, a method for studying the electronic structure of transition-metal systems, in which a plane-wave expansion for the sp electrons is augmented with a Gaussian basis set to describe the relatively more localized d shell (the mixed-basis pseudopotential method) has been formulated.[12] It is worth noting that the mixed-basis procedure, as presently formulated, requires a momentum-space representation of the Gaussian basis function for the calculation of various matrix elements coupling these functions through the single-particle Hamiltonian. The application of this procedure to transition elements in the $3d$ series requires a prohibitively large plane-wave expansion to describe these Gaussian basis functions accurately, since the d states are particularly strongly localized in the core region in this series. For example, in the case of Cu in the fcc crystal structure, with which we will be concerned in this paper, the peak of the d-state charge density is at 0.16 of the Wigner-Seitz cell radius, so that an accurate description of an appropriate Gaussian function which could represent the d shell would require an expansion in nearly 10^4 plane waves.

In this paper we present a reformulation of the mixed-basis method that is particularly suitable for studying the electronic structure of elements in the $3d$-transition series, in which the unscreened $3d$ pseudopotential is particularly strong. However, we note that the methods outlined here are also useful for studying the electronic structure of the heavier transition metals, where the d pseudopotential is substantially weaker;[13,14] in this latter case the principal advantage of our method is the efficiency with which the localized basis functions in the expansion set are treated.

Our approach to the mixed-basis expansion makes use of a real-space representation of the localized basis functions. As described in detail below, we derive an optimized set of basis functions with d symmetry, which are designed to provide a description of the full valence d wave function with the fewest number of auxiliary plane waves. An important aspect of the choice of localized basis function is that they vanish outside a critical radius chosen so that the functions are nonoverlapping in the solid state. This simplifies the calculation of many matrix elements involving the localized basis functions tremendously. Techniques for computation of matrix elements and the construction of an output charge density which

we have found particularly useful for this application will be presented below.

As an example we have applied the method to study the electronic and structural properties of the cubic phases of elemental Cu. Structural energy calculations employing the mixed-basis pseudopotential scheme have recently been carried out for the two heavier noble metals, Ag and Au.[13] For Cu we find that the fcc structure is slightly energetically favored over the bcc structure, in agreement with the experimental stability of fcc Cu. For the fcc structure we find an equilibrium density and bulk modulus in good agreement with experiment. For the bcc structure, we find that compression of the crystal gives rise to an interesting symmetry-breaking relaxation of the filled d shell, which is apparently not possible in the close-packed fcc structure. In our studies the total energy of the fcc phase is lower than the total energy of the bcc phase at all densities considered. However, we find that the bcc structure can attain an anomalously stable "high-density" form whose free energy may be competitive with the fcc structure at finite temperature.

The plan of this paper is as follows. In Sec. II the localization of the valence d orbitals in Cu is considered, and a method for representing the valence d function in the solid state is presented. In Sec. III the self-consistent valence-band structure is presented for Cu in the fcc structure and compared with the results of present state-of-the-art calculations. The band structure of the hypothetical bcc structure will also be presented. in Sec. IV the total energies of the two crystal structures are calculated and compared. In Sec. V the self-consistent charge densities and their variation upon compression of the two crystal structures are calculated and compared. Finally, a number of technical points relating to the use of our real-space optimized mixed-basis function in a band-structure code will be presented in the Appendixes, which will be helpful to readers who will wish to make use of these functions in numerical calculations.

II. OPTIMIZED LOCAL BASIS FUNCTIONS

In this section we discuss the procedure for constructing the "optimized" local basis functions which are used in our formulation of the mixed-basis method. These basis functions are required (1) properly account for the behavior of the valence electrons near the core region of the pseudoatom, and (2) to not overlap nearest-neighbor local basis functions. The nonoverlapping feature of the basis functions provides many computational advantages. For example, many of the matrix elements simplify to single-term, one-dimensional integrations and/or are wave-vector independent.

Though there are many ways to derive a numerical fitting scheme, the procedure outlined below is presented in a way that highlights the physical motivation. The nomenclature "optimized" derives from the numerical advantages of the localized basis functions and from the maximal use of the variational freedom provided by the atomic-function—plane-wave basis set.

We start with a set of radial atomic (pseudo) wave functions, $f_i^{\text{atomic}}(r)$, that are obtained as numerical solutions of the pseudopotential radial Schrödinger equation. We use the Cu pseudopotential of Bachelet *et al.*[5] which is shown in Fig. 1(a). The depth of the d pseudopotential and its shape near the core is typical of d pseudopotentials for transition metals in the $3d$ series and makes Gaussian or plane-wave equations of the potential matrix elements impractical. This has been a contributing factor to the lack of pseudopotential electronic structure calculations for these elements.[15,16]

By construction, the numerically obtained radial functions will accurately represent the behavior of the d electrons in the core region of the pseudoatom. It is important to reproduce this "near-core" behavior in the crystal to determine accurately the position of the d states relative to the sp states. These atomic functions are peaked close to the nucleus [Fig. 1(b)] and thus have many high Fourier components. However, these functions have long exponential tails and are inconvenient to use as part of the mixed basis in the crystal calculations because they spatially overlap, thereby enormously complicating the evaluation of matrix elements. In fact in the opposite limit, basis functions that are short ranged such that there is no overlap between functions centered at nearest-neighbor sites are very effective computationally. Bloch function matrix elements of the kinetic energy and the short-ranged, nonlocal potential reduce to atomic calculations

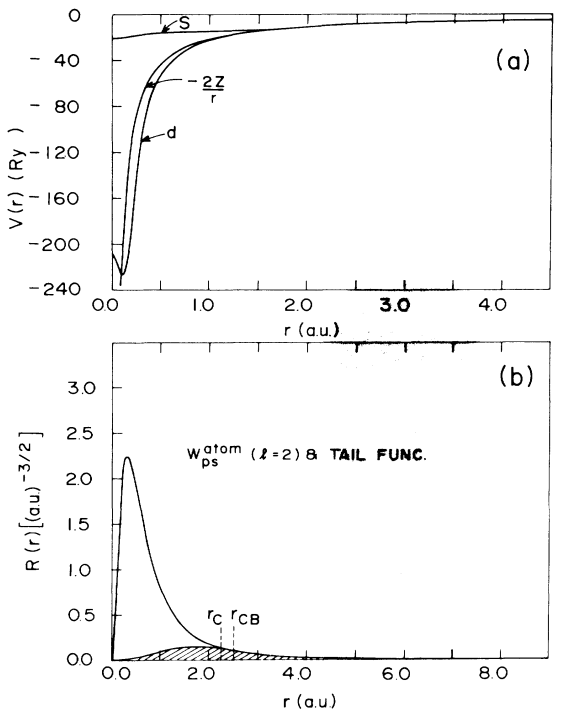

FIG. 1. (a) Unscreened ion potential, and $l=0,2$ valence ion pseudopotentials for Cu, following Bachelet-Hamann and Schlüter (Ref. 5). (b) Radial part of valence pseudo-wavefunction for $l=2$ state in Cu; the shaded region indicates the tail function which is well described by an expansion with a few long-wavelength plane waves. r_{CB} is the Wigner-Seitz cell boundary, and r_c is the cutoff radius described in the text.

that are independent of the crystal structure and wave vector. The details of the matrix-element evaluations are contained in Appendix A.

The computational simplicity provided by localized (nonoverlapping) functions motivates our attempt to remove the "exponential" tails without damaging the near-core behavior of the radial functions. This is accomplished by subtracting a smooth "tail" function from the atomic function:

$$f^{\text{opt}}=f^{\text{atomic}}-f^{\text{tail}} , \tag{1}$$

where, ideally, the tail function is identical to the atomic wave function beyond a "cutoff" radius, r_c, and smoothly approaches zero at the origin. For each type of atom in the unit cell, a sphere radius is chosen so that the spheres (centered at the atomic positions) do not overlap. To achieve the numerical benefits described above, the cutoff radius should fit inside the Wigner-Seitz sphere about the atom of interest. To allow for changes in the lattice constant in the present work, r_c was taken about 10% smaller than the largest nonoverlapping sphere radius.

The basis set we use for the expansion of the crystalline wave functions is a mixture of plane waves and Bloch sums containing these optimized functions for the d orbitals of Cu. It is known from previous work[17] that atomic Bloch functions augmented by plane waves provide a satisfactory basis set for accurate charge densities for systems with various types of bonding, e.g., metallic, covalent, ionic, etc. In order that our "optimized" basis set has the same variational flexibility as the atomic-function—plane-wave basis set, we require that the tail functions, f^{tail}, have no spatial Fourier components outside the range of the plane-wave part of the basis set. Thus we construct f^{tail} from a set of slowly-varying plane waves.

In general, the radial part, $f(r)$, of a function of angular momentum l and maximal wave vector $Q_{\max}$ can be represented by its Bessel transform (radial part of Fourier transform):

$$f(r)=\int_0^{Q_{\max}} F(Q)j_l(Qr)Q^2dQ . \tag{2}$$

We construct a tail function by fitting it to the atomic radial function in a region between r_c and $r_{\max}$, where r_c is chosen somewhat inside the Wigner-Seitz radius and $r_{\max}$ in practice extends to second- or third-nearest neighbors. Our strategy, then, is to adjust the transform coefficients, $F^{\text{tail}}(Q)$, to obtain a best least-squares fit of the atomic function, $f^{\text{atomic}}(r)$, in a region from r_c to $r_{\max}$. We approximate the integral in (2) so that

$$\begin{aligned} f^{\text{tail}}(r)&=\int_0^{Q_{\max}} F^{\text{tail}}(Q)j_l(Qr)Q^2dQ \\ &\approx \sum_{j=1}^{N_G} F^{\text{tail}}(Q_j)j_l(Q_jr)Q_j^2\Delta Q_j . \end{aligned} \tag{3}$$

The least-squares minimization condition

$$\frac{\partial}{\partial F^{\text{tail}}(Q_j)}\int_{r_c}^{r_{\max}}[f^{\text{tail}}(r)-f^{\text{atomic}}(r)]^2r^2dr=0 \tag{4}$$

leads to a set of linear equations:

$$\sum_k F^{\text{tail}}(Q_k)B_{kj}=D_j \tag{5}$$

to be solved for $F^{\text{tail}}(Q_k)$, where

$$B_{kj}=\int_{r_c}^{r_{\max}} j_l(Q_kr)j_l(Q_jr)r^2dr\,Q_k^2\Delta Q_k \tag{6}$$

and

$$D_j=\int_{r_c}^{r_{\max}} f^{\text{atomic}}(r)j_l(Q_jr)r^2dr . \tag{7}$$

Because of the restricted range $(r_c,r_{\max})$ over which the integrations are performed, the $j_l(Q_jr)$ for a discrete set of Q_j form a nearly-linearly-dependent set. This makes the matrix B_{jk} difficult to invert. To remove this difficulty, we transform to an orthogonal expansion set formed from the normalized eigenvectors of the matrix B_{jk}, which have the form

$$h_\mu(r)=\sum_{j=1}^{N_Q} A_{\mu j}j_l(Q_jr) . \tag{8}$$

The irrelevant degrees of freedom are removed by discarding eigenvectors of B_{jk} whose eigenvalues are smaller than a cutoff value, say 10^{-3}. From the theory of orthogonal functions on an interval, it can be shown that the best n-parameter approximation to a well-behaved function is obtained by the Fourier series expansion of the function, terminated at the nth term. Thus Eq. (3) is replaced by

$$f^{\text{tail}}(r)=\sum_{\mu=1}^{n} C_\mu h_\mu(r) , \tag{9}$$

where

$$C_\mu=\int_{r_c}^{r_{\max}} f^{\text{atomic}}(r)h_\mu(r)r^2dr . \tag{10}$$

Since the h_μ are composed of low-frequency Bessel functions, the analytic continuation of f^{tail} outside the interval $(r_c,r_{\max})$ is guaranteed to approach zero smoothly towards the origin and decay rapidly toward zero beyond r_c. After constructing f^{opt} from Eqs. (1), (9), and (10), we impose the normalization

$$\int_0^\infty |f_i^{\text{opt}}(r)|^2r^2dr=1 . \tag{11}$$

The tail function for Cu d orbitals constructed from the procedure just described is shown as the shaded region in Fig. 1(b).

This procedure, in which we extract a set of localized basis function which are nonoverlapping in real space bears some resemblance to the "quasiatomic" orbitals derived by Bendt and Zunger.[18] In that application the quasiatomic orbitals are self-consistent solutions to an atom which is confined within a Wigner-Seitz sphere. In our case the localized functions are obtained from the self-consistent solution to the full pseudoatom (with no boundaries, but with the long-wavelength plane-wave part removed). Although one might expect the residual component of Bloch function to be more rapidly convergent following our scheme, the philosophy underlying the two models is very similar. Details concerning matrix-element evaluation, and schemes for accumulating the charge density which we have found particularly useful are tabulated in the Appendix.

III. TEST ON BAND STRUCTURE OF COPPER

We chose copper as a test material for our new formalism. As mentioned earlier, copper is a $3d$ transition metal and the corresponding d pseudopotential is very strong, which makes both a plane-wave expansion or an ordinary mixed-basis calculation difficult due to the high localization of the d-electron wave function. Therefore, it is not very surprising that there have been no rigorous plane-wave-based pseudopotential calculations for copper.[15,16] We have obtained several interesting results in this study which confirm the accuracy of the method, and find one unexpected aspect in the structural behavior of Cu.

There are several parameters to be chosen before the main calculation. In the calculation discussed below we employed around 60 to 80 plane waves (cutoff energy $E_1 = |\mathbf{k}+\mathbf{G}|^2_{\max} = 15$ Ry) for the plane-wave part of the basis function set, around $3K$ reciprocal-lattice vectors ($E_2 = |\mathbf{G}|^2_{\max} = 169$ Ry) to expand the relatively smooth local potential in the band calculation, around $12K$ reciprocal-lattice vectors ($E_3 = |\mathbf{G}|^2_{\max} = 430$ Ry) to expand the charge density, and 512 $\mathbf{k}$'s in the Brillouin zone [equal to 29 $\mathbf{k}$'s in irreducible BZ (IBZ) of fcc structure] to construct the charge density with the Gaussian weighting scheme that is very efficient to accelerate the convergence of the total energy with respect to the number of $\mathbf{k}$ points.

In the mixed-basis approaches the number of plane-wave basis functions is the most important parameter because the completeness of the basis set should be required before expanding any function with a basis set. Using the three different cutoff energies ($E_{1a} = 10$ Ry: around 50 plane waves; $E_{1b} = 15$ Ry: around 70 plane waves; and $E_{1c} = 17$ Ry: around 90 plane wave), we have calculated the eigenvalues and the total energies of fcc copper at the reference unit-cell volume to test the convergence with respect to the number of plane-wave basis functions in the set. The differences in the eigenvalue Γ_1, Γ_{25} and the total energy between E_{1a} and E_{1b} are 0.013, 0.090, and 10.2 mRy, respectively; and for E_{1b} and E_{1c}, 0.005, 0.002, and 4.1 mRy, respectively. As far as we are concerned with eigenvalues, we can conclude that we have already reached a very good convergence at the cutoff energy $E_1 = 15$ Ry.[13,14] For the total energy, although it is too small to be compared to the cohesive energy of copper (equal to 256 mRy), the difference of 4.1 mRy is not so satisfactory. However, we have found that this total-energy shift between the different cutoff energies is nearly constant when we calculate the total energy as a function of the unit-cell volume.[13] As a result, the ground-state bulk properties are very stable to the change of cutoff energy E_1 (the relative changes in the equilibrium lattice length are within 0.3%, and for the bulk modulus, within 3.2%). Therefore, we chose the cutoff energy $E_1 = 15$ Ry.

The number of the reciprocal-lattice vectors determined by the cutoff energy E_3 is also a parameter of importance, especially in dealing with $3d$ transition metals, because of the strongly localized d electron density. The total charge density is expanded by these plane waves in $\mathbf{G}$ space and they are directly related to the size of the uniform mesh in $\mathbf{R}$ space as shown in Appendix C. When we increase the number of plane waves from 7.5 K ($E_3 = 315$ Ry) to 10 K ($E_3 = 390$ Ry), the total energy is lowered by 1.50 mRy; from 10 to 12 K ($E_3 = 430$ Ry), by 0.48 mRy; and from 12 to 14 K ($E_3 = 470$ Ry), by 0.13 mRy. The final difference is likely to be in the category of acceptable convergence in the current calculation, and so we used the cutoff energy $E_3 = 430$ Ry to calculate the charge density in $\mathbf{G}$ space and the total energy.

In Fig. 2 we show the band structure along the symmetry lines L-Γ-X at the equilibrium lattice constant. A separate table of eigenvalues of each high-symmetry $\mathbf{k}$ points, for more quantitative comparison to other theoretical results and experimental data, is given in Table I. The present results are comparable to earlier calculations that were also based on local-density-approximation (LDA).[19,20] It is interesting to note that the entire dispersion of the d bands which occurs in this model is provided by the mixing of our nonoverlapping d functions with a relatively small set of plane waves which penetrate the cores and couple the d-like degrees of freedom on each atomic site. In accord with other calculations, the present results show the general trend that the LDA yields d bands that are too high and too dispersive relative to the data obtained by photoemission experiments.[21] Some authors explain these differences between LDA results and experiment by including self-interaction and metallic screening effects and reported some improved results.[20,22]

In Fig. 3 we show the analogous band structure for bcc copper along the symmetry line N-Γ-H at the same volume per atom to the experimental fcc one. The result is relevant to the discussion in Sec. V; it shows that even in the bcc structure, the d bands remain completely occupied.

IV. COMPUTED PROPERTIES OF COPPER

Since the band structure compares favorably with the results of other state-of-the-art methods, we would like to

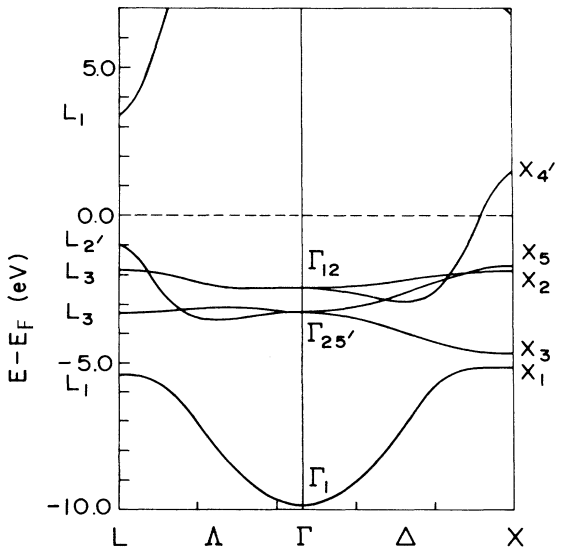

FIG. 2. Band structure for Cu in the fcc structure ($a = 6.822$ a.u.) along high-symmetry directions in the Brillouin zone.

TABLE I. Band energy comparison for fcc copper (eV). Results of three self-consistent LDA calculations and one angle-resolved photoemission experiment. Band positions are given relative to the Fermi energy ($\epsilon' = E_f - \epsilon$).

	KKR[a]	LAPW[b]	Present[c]	Expt.[d]
Γ_{12}	2.41	2.40	2.45	2.85
$\Gamma_{25'}$	3.24	3.20	3.27	3.65
Γ_1	9.42	9.47	9.88	
X_5	1.62	1.64	1.70	2.05
X_2	1.82		1.89	
X_3	4.68		4.69	4.50
X_1	5.27	5.07	5.18	5.20
$L_{2'}$	1.14		0.98	0.90
L_3	1.78	1.80	1.86	2.25
L_3	3.29		3.32	3.65
L_1	5.25	5.23	5.41	
Γ_{12}-$\Gamma_{25'}$	0.83	0.80	0.82	0.80
X_5-X_1	3.65	3.43	3.48	3.15
L_3-L_1	3.47	3.43	3.55	

[a]Korringa-Kohn-Rostoker calculation with LDA (Ref. 19).
[b]Linear augmented-plane-wave calculation with LDA (Ref. 20).
[c]This result was obtained at the lattice constant $a_0 = 6.822$ a.u.
[d]Reference 21.

extend the method to study the zero-temperature-state structural properties of bulk copper such as crystal structure, equilibrium lattice constant, cohesive energy, bulk modulus, etc. The bcc structure is not observed for copper, implying that the total energy of the fcc structure is less than that of the bcc. Accordingly, it is interesting to make and compare theoretical predictions for the energy of the two structures. To make this comparison we must evaluate the total energy as a function of unit-cell volume for each structure and then choose the lower-energy structure as the ground state of the system. For self-consistency, an accuracy of 0.01 Ry in eigenvalues is sufficient for calculating the band structures. However, the total-energy variation around the equilibrium volume is so small that the energy fluctuation between successive iterations should be less than that energy difference in order to yield a reasonably smooth energy curve. The required accuracy in the current calculation is of the order of 0.1 mRy. The total energy of the crystal is calculated using the momentum-space formalism given by Ihm, Zunger, and Cohen.[23]

A. fcc copper

We evaluated the total energies of fcc copper at various lattice constants ranging over a ±4% expansion and compression of the lattice constant. The results are shown in Fig. 4. Some static ground-state properties of bulk can be obtained directly from this total-energy curve. Table II contains the calculated and experimental equilibrium lattice constant, cohesive energy, and bulk modulus.

The agreement of our results with experiment is quite good. The other theoretical data in Table II were all based on all-electron LDA calculations.[18,23] Our results indicate that the pseudopotential formalism remains accurate even for transition metals with a localized valence d shell, and that use of cutoff localized basis functions is practical and effective. To calibrate the efficiency of this scheme, the calculation requires approximately 10 CPU seconds per **k** point per iteration to obtain these results on an IBM-3081. The energy value is stable within 0.01 mRy, which yields a very smooth total-energy curve. In other words, we can deal with a very small energy difference between any two energetically similar systems. This led us to try to compare the structural energy difference between the fcc structure in nature and a hypothetical bcc crystal structure for copper.

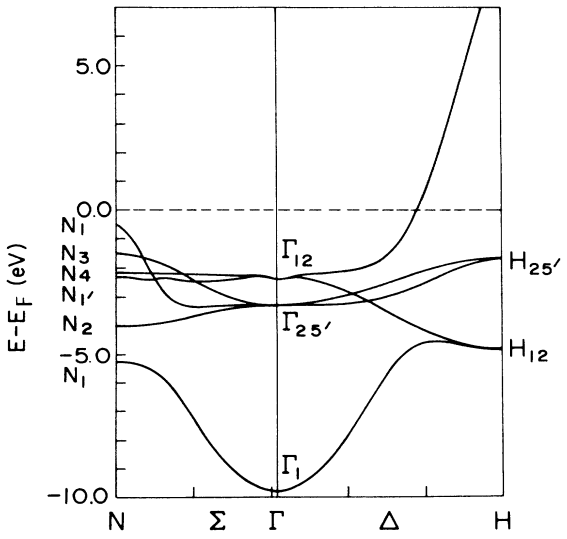

FIG. 3. Band structure for Cu in the bcc structure ($a = 5.420$ a.u.) along high-symmetry directions in the Brillouin zone.

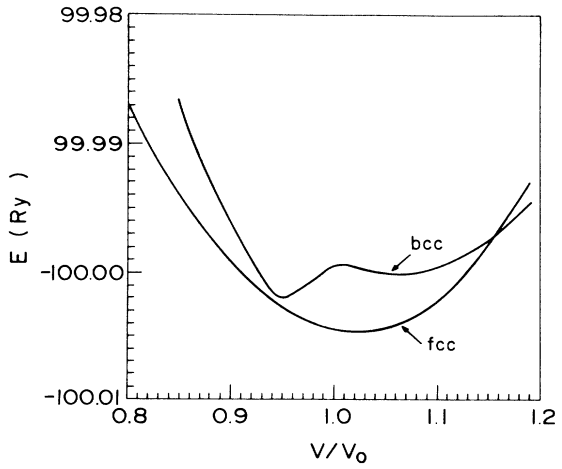

FIG. 4. Total energy for Cu as a function of reduced volume for the fcc and bcc crystal structures. V_0 is the volume of the primitive cell corresponding to the experimentally observed bulk density of fcc Cu.

TABLE II. Bulk property comparison for fcc copper. Equilibrium lattice constants, cohesive energies, and bulk moduli obtained from several calculations and experiments are compared.

	KKR[a]	ASW[b]	Present	Expt.[c]
Lattice constant (a.u.)	6.76	6.81	6.85	6.81
Cohesive energy (Ry/atom)	0.301	0.298	0.246	0.257
Bulk modulus (Mbar)	1.55	1.29	1.50	1.42

[a]Reference 19.
[b]Augmented-spherical-wave calculation (Ref. 24).
[c]Reference 25.

B. bcc copper

A phase transformation of copper from fcc to bcc is not observed experimentally. Nonetheless, it is interesting to compute the energy difference between the two phases. In this respect, a calculation of this type can explore behavior outside the range of present experiment.

We need to evaluate the total energy of bcc copper using a basis comparable to that employed for fcc calculations in order to compare the energy difference between the two phases in a meaningful way. We used the same plane-wave cutoffs for the wave functions, potential, and charge density, and a total of 512 **k** points in Brillouin zone (30 in irreducible sector). We take a reference structure with $a^{\rm bcc}=a^{\rm fcc}_{\rm expt}/2^{1/3}$ so that the atomic densities of each reference structure are the same. The results are given in Fig. 4. The total-energy curve in the bcc phase shows an unexpected double minima, one at a 7% volume expansion and the other at a 6% volume compression. We verified the shape of this total-energy curve by making calculations for 12 intermediate densities; the results yield a smooth curve without any significant scatter. As we compress the system, it reaches the shallow first minimum. Upon further compression the system suddenly goes down to the deep second minimum and reaches its "stable" bcc structure. We checked the convergence of these results with respect to the number of plane waves in the basis set by expanding the cutoff energy E_1 to 20 Ry (approximately 140 plane waves). The results showed an increase in the cohesive energy by approximately 5 mRy, but a very similar bimodal shape for the structural energy curve was obtained. This is consistent with our estimates of the convergence of the results with respect to the basis-set size noted in Sec. III. In the next section we will give a microscopic description of this phenomenon in bcc copper. However, before doing so we emphasize that the present calculation shows that fcc copper is slightly more stable than the bcc structure. The energy difference between the absolute minima of the two structures is 3 mRy, and at the volume where bcc structure has its absolute minimum, the energy difference between fcc and bcc is about 0.6 mRy. Because the minimum part of the bcc energy curve never intersects with the fcc curve, we do not expect a pressure-induced phase transition to the bcc structure at zero temperature.

V. VALENCE CHARGE DENSITIES

The unusual behavior of the total energy of Cu in the bcc structure shown in Fig. 4 can be traced to specific features in the valence charge density. In this section we will examine and compare the self-consistent charge densities obtained in the fcc and bcc crystal structures.

In Fig. 5 we present the total valence charge density for Cu in the fcc crystal structure at the equilibrium density. The lines are contours of constant density in the (111) plane. The accompanying linear plot gives the values of the charge density on a cut through the $[1\bar{1}0]$ direction. There are two features to notice on these graphs. First,

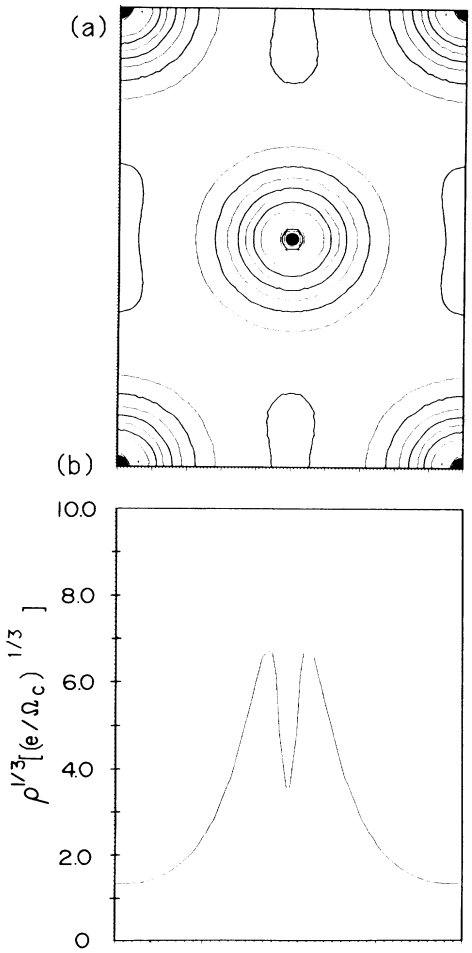

FIG. 5. Total valence charge density for Cu in the fcc structure with $a=6.822$ a.u. (top) Contours of constant charge density in the (111) plane; (bottom) linear plot along the $[1\bar{1}0]$ direction in the (111) plane.

there is a large peak in ρ at 0.3 a.u. away from the Cu nucleus arising from the peak of the localized d contribution to the charge density. Secondly, the nearly-free sp electrons make a much smaller smooth contribution to ρ which can be seen most clearly in the interstitial regions. The d bands in the crystal are completely occupied, and as a consequence the d density is nearly spherical, as can be seen in the contour plots of Fig. 5(a).

A similar situation is found for the total valence charge density in the bcc structure at the same atomic density, as shown in Fig. 6. The upper plot is a contour map in the (110) plane of the bcc crystal, the lower linear plot provides quantitative data on a cut along the [001] direction. Again we see the characteristic sharp d peak in the core region, and a smooth free-electron contribution in the interstitial region. The d bands are completely occupied in this structure (see the band structure in Sec. III), and the net d contribution to the charge density is nearly spherical.

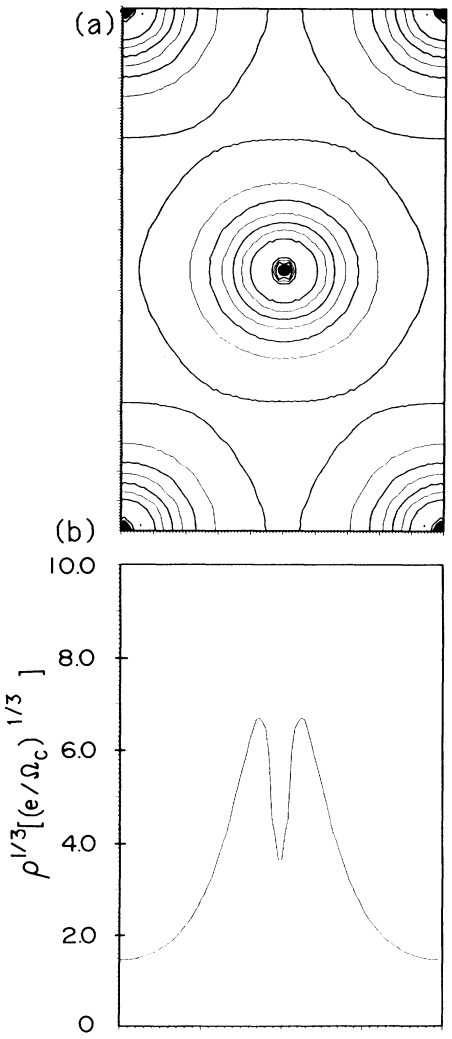

FIG. 6. Total valence charge density for Cu in the bcc structure with $a=5.420$ a.u. (a) Contours of constant charge density in the (110) plane; (b) linear plot along the [001] direction in the (110) plane.

We are interested in examining relatively subtle changes in the valence charge distribution as these two crystal structures are expanded and compressed. A strategy for doing this is to examine the behavior of a difference charge density, in which we normalize out the simple effect of changing the volume of the unit cell. Specifically, we examine a local charge difference function:

$$\delta q_{1-2}(r_{ijk})=\frac{1}{N}[\rho_1(r_{ijk})\Omega_1-\rho_2(r_{ijk})\Omega_2]\ , \tag{12}$$

where N is the number of grid points on a real-space mesh used to represent the valence charge density, r_{ijk} is a *dimensionless* grid point within the unit cell, the indices 1 and 2 represent two densities between which the charge densities are to be compared, and the Ω_i are the unit-cell volumes of the two structures. The quantity calculated in Eq. (12) represents the charge density at the ijkth mesh point in the unit cell, and allows us to focus on the relative distribution of charge in the cell for two crystals with different densities. By construction, δq is a quantity which integrates to zero.

We first consider the effects of compression of the fcc structure. Figures 7(a) and 7(b) present contours of constant δq [again in the (111) plane] in the fcc structure. The upper figure demonstrates the effect of compression from an *expanded* lattice constant ($a=7.095$ a.u.) to the equilibrium lattice constant ($a=6.822$ a.u.). The dashed contours are negative values of δq, the solid contours are positive. Our point here is that there is no *distortion* of the shape of the charge density contours on compression, indicating that the d contribution is spherical at both densities. (The apparent shift of charge within the core region is misleading, in that a perfectly rigid core, examined in this way at two different crystal densities would also show a similar shift of charge from the inner to outer regions.) A similar behavior is illustrated in Fig. 7(b) where the change in valence density upon 2% contraction of the lattice constant, relative to the equilibrium volume, is examined ($a=6.685$ a.u. in the compressed structure). The most substantial changes are again found in the core region, and reflect a rigid movement of the d-charge density towards the boundaries of the Wigner-Seitz cell. In summary, the charge difference plots exhibit nearly spherically symmetric behavior in the core region, as would be expected if the d bands remain fully occupied at all the crystal densities studied.

Similar calculations for the bcc structure reveal a rather different systematic behavior. Figures 8(a) and 8(b) presents the analogous contour plots of constant difference density. In Fig. 8(a) we compared the charge density in the bcc structure that has the same density as the fcc equilibrium structure with the charge density found for a 4% expansion of the cell volume. For weak compression, we again observe a systematic migration of the d-band density towards the boundaries of the Wigner-Seitz cell. However, even for weak compression we see that this expansion is not spherically symmetric, but is oriented preferentially towards the interstitial regions along the [001] directions. This behavior is demonstrated much more

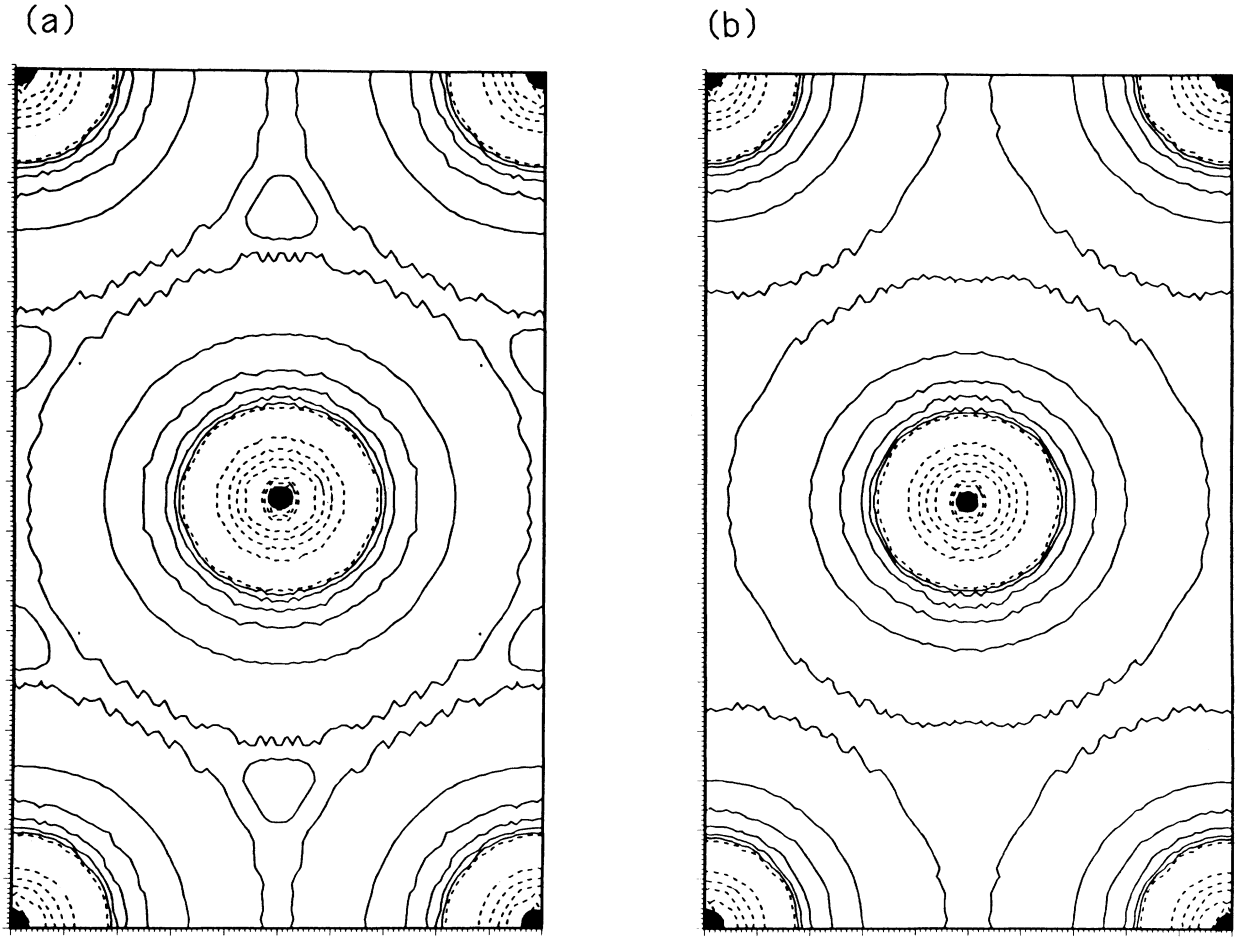

FIG. 7. Difference charge densities illustrating the effect of compression on the total charge density in the (111) plane for Cu in the fcc structure. (a) The charge density for a 4% expansion of the lattice constant is subtracted from the charge density at equilibrium. (b) The charge density at equilibrium is subtracted from the charge density for a 2% contraction.

dramatically, if we consider the effects of a 2% compression of the lattice constant from a reference density in which the bcc structure has the same density as the fcc structure, shown in Fig. 8(b). Here we see two well-defined lobes oriented along the [001] direction, showing that the d shell is being driven out of spherical symmetry by the uniform compression.

An important consequence of this symmetry breaking is that the projection of the d-charge density onto the nearest-neighbor [111] directions is reduced in the compressed bcc structures. This allows the crystal to attain a slightly higher density, with a corresponding increase of the cohesive energy, as illustrated in Fig. 4. The secondary minimum develops as the tails of the d shells overlap and the distortion of the density becomes more pronounced. This asymmetry is unexpected since the d shell remains fully occupied in all of the crystal volumes considered. However, it is well known that there is substantial hybridization between the $3d$ shell and the nearly free sp band in the solid state; we believe this behavior is due to the resonant mixing of d character into the higher-lying unoccupied free-electron band as the crystal is compressed. We know of no previous observation of similar behavior in the heavier noble metals, Ag and Au, although the systematics of this kind of behavior in the heavier systems would be interesting to examine. This behavior is not observed in compression of the noble metals in the fcc structure; we believe that the fcc close-packed structure offers less "interstitial volume" for this asymmetric compression, and thus the $3d$-valence shell remains nearly spherical upon compression of the fcc structure.

VI. SUMMARY

We have developed a real-space reformulation of the mixed-basis pseudopotential method. The method is especially convenient for systems in which there is relatively strong localization of a component of the valence charge density, so that a conventional plane-wave expansion is

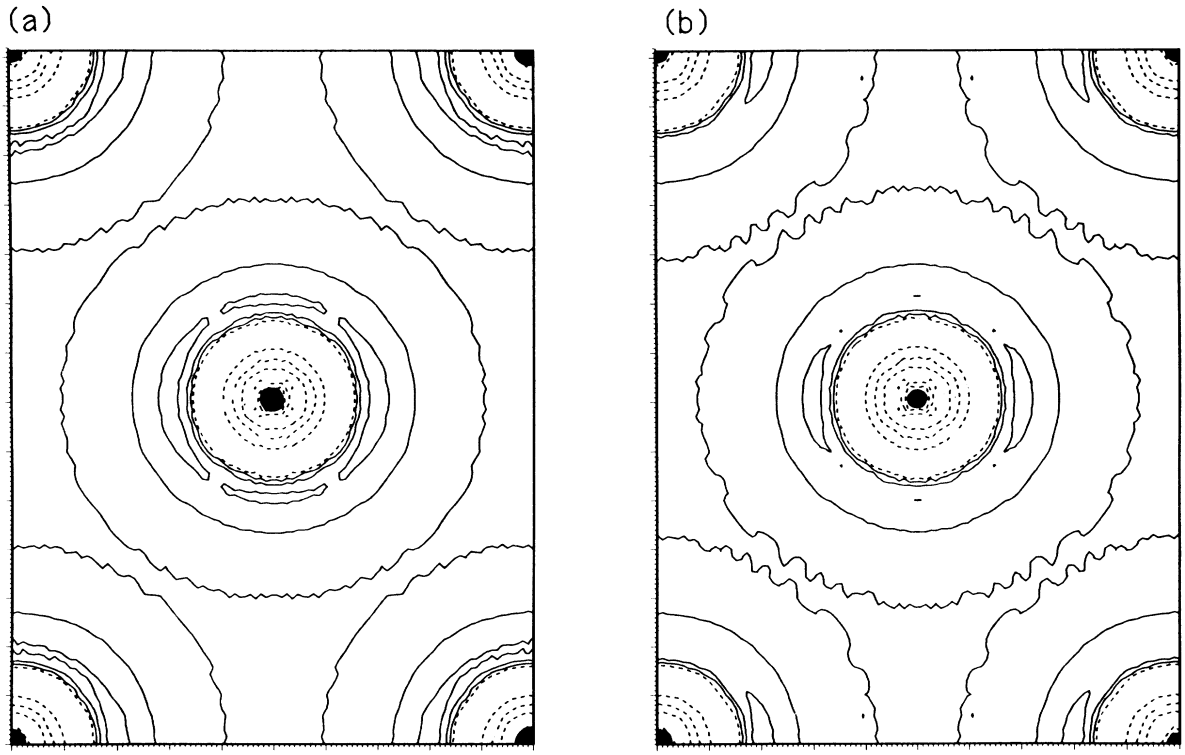

FIG. 8. Difference charge densities illustrating the effect of compression on the total charge density in the (110) plane for Cu in the bcc structure. (a) The charge density for a 4% expansion of the lattice constant is subtracted from the charge density at $V/V_0=1$. (b) The charge density for $V/V_0=1$ is subtracted from the charge density for a 2% contraction of the lattice constant.

not practical. This method augments a small plane-wave expansion with a small number of nonoverlapping real-space basis functions, from which matrix elements can be calculated by **k**-independent one-dimensional quadrature in most cases. The method is essential for accurately dealing with the strong $l=2$ potential in the $3d$ transition series, and may provide a more efficient scheme for describing the heavier transition elements, some of which have already been studied with the "conventional" Gaussian mixed-basis method.

We have tested the scheme by calculating the electronic structure and bulk structural properties of elemental Cu. We find that the results are of comparable quality to other state-of-the-art methods. We find that Cu is stable in the fcc crystal structure, the lattice constant is recovered to 0.6% accuracy, while the error in the bulk modulus is 6%. The fcc structure is slightly energetically favored over a bcc structure at an equivalent density. Compression of the bcc structure produces an anomalously stable high-density form of bcc Cu in which the valence d shell develops a nonspherical distortion.

The modified mixed-basis method is quite efficient, and offers the possibility of high-quality calculations on the structural properties of more-complicated cells to study surface and defect structure. Generalization of the scheme to study high-symmetry phonon frequencies in bulk Cu are in progress.

ACKNOWLEDGMENTS

We would like to thank K. Ho, D. Vanderbilt, and A. Williams for several very helpful discussions. This work was supported by the National Science Foundation through the Materials Research Laboratories Program under Grant No. DMR 84-14640. E.J.M. acknowledges additional support by the Alfred P. Sloan Foundation.

APPENDIX A: HAMILTONIAN AND OVERLAP MATRIX ELEMENTS

1. Hamiltonian

The many-electron Schrödinger equation is reduced to a one-particle equation by use of effective potentials that are derived from the local approximation to the exchange and correlation energy density functionals.[2] We solve the one-electron equation in a mixed (nonorthogonal) basis of plane waves and linear combination of atomic orbital (LCAO) functions. This is essentially the method of Louie, Ho, and Cohen.[12] The key feature of our approach is the use of *nonoverlapping* localized basis functions that represent the tightly bound d electrons without complicating the evaluation of matrix elements. The nonoverlapping character of the localized functions leads to the simplification of the local-local matrix elements described in

Ref. 12 without the approximation used there. For this reason, we will review the mixed-basis technique of Louie, Ho, and Cohen and point out the differences where appropriate.

The one-electron Hamiltonian can be written as

$$\mathbf{H}=T+V_{\rm ps}^{\rm ion}+V^{H}+V^{\rm xc}\ , \tag{A1}$$

where T is the kinetic energy operator, $V_{\rm ps}^{\rm ion}$ is the ionic pseudopotential describing the valence-electron—ion attraction, and V^H and $V^{\rm xc}$ are the Hartree and exchange-correlation parts of the electron-electron interaction. The ionic pseudopotential can be divided into local and nonlocal (angular-momentum-dependent) parts:

$$V_{\rm ps}^{\rm ion}=U^{\rm loc}+U^{\rm nl}\ ,$$

where the nonlocal part is a sum of radial functions times angular momentum projectors:

$$\langle\,\mathbf{r}\,|\,U^{\rm nl}\,|\,\mathbf{r}'\,\rangle=\frac{\delta(r-r')}{r^2}\sum_{L'}Y_{L'}(\mathbf{r})U_{l'}^{\rm nl}(r)Y_{L'}(\mathbf{r}')\ .$$

The ionic pseudopotential for bulk Cu is a lattice sum of atomic Cu pseudopotentials. We use an analytic Fourier transform of the Cu pseudopotential parametrized by Bachelet, Hamann, and Schlüter.[5] The s and d pseudopotentials are shown in Fig. 1(a).

The Hartree potential V^H is related to the pseudo-valence-charge-density:

$$\nabla^2V^H(\mathbf{r})=-4\pi e^2\rho(\mathbf{r})\ . \tag{A2}$$

The exchange-correlation operator is represented by a local potential $V^{\rm xc}$. We make use of the results of Ceperley and Alder[3] in the parametrized form given by Perdew and Zunger.[4] This operator is evaluated using a real-space representation of the charge density.

We begin the self-consistent procedure using a superposition of the atomic charge densities to represent the charge density in the solid. Then the matrix elements are evaluated and we solve for the wave functions $\Psi_{n\mathbf{k}}$, where n is the band index. A new charge density is obtained by summing over the filled states

$$\rho'=\sum_{n,\mathbf{k}}^{\rm occupied}|\,\Psi_{n\mathbf{k}}\,|^2$$

of approximately 30 wave vectors in an irreducible sector ($\frac{1}{48}$th) of the Brillouin zone. To identify the filled states, the Fermi level is found by estimating the density of states from the computed eigenvalues. A Gaussian weighting scheme is used to give a reasonable interpolation of the zone integration for both the density of states and the charge density.[13]

To avoid drastic oscillations from iteration to iteration a 3/7 mixing ratio of the present and previous charge densities is used to obtain a charge density from which the new Hartree and exchange-correlation potentials are computed. Because the form of the operators are the same, the new potential are combined with the local part of the ionic pseudopotential:

$$V^{LH\rm xc}=U^{\rm loc}+V^H[\rho]+V^{\rm xc}[\rho]\ ,$$

where we have indicated that the Hartree and exchange-correlation potentials are functionals of the density. The combined potential is somewhat smoother in real space than either the Hartree or local ionic potentials alone. This reduces the size of the reciprocal-space expansion from which matrix elements are calculated.

2. Matrix-element evaluation

The nonorthogonal basis set leads to the generalized matrix equation

$$(H-ES)\Psi=0\ .$$

We will develop expressions for the matrix elements under the assumption that there are several atomic species in the crystal but only one atom of each species within the unit cell. This assumption provides adequate generality without unduly complicating the algebra. In addition, for notational simplicity we assume that the optimized atomic functions on a given site have the same orbital angular momentum.

Our basis set divides into two parts, plane-wave and local functions, and accordingly the matrix elements can be divided into three types: plane-wave—plane-wave, plane-wave—local, and local—local. In the following, the symbol L denotes the angular momentum quantum numbers (l,m) τ_p is the position of the pth atom in the unit cell, $\phi_{p,L}$ is an LCAO formed from a localized function of angular momentum L at τ_p within the unit cell, $\mathbf{G}$ is a reciprocal-lattice vector, $\mathbf{k}$ is a Brillouin zone wave vector, and $|\,\mathbf{k}+\mathbf{G}\,\rangle$ is a plane-wave basis function. The Bloch basis functions $\phi_{p,L}$ are constructed from the optimized (i.e., nonoverlapping) atomic functions:

$$\phi_{p,L}=\frac{1}{\sqrt{N}}\sum_{\mathbf{R}}f_{p,l}(\,|\,\mathbf{r}_p-\mathbf{R}\,|\,)Y_L(\mathbf{r}_p-\mathbf{R})e^{i\mathbf{k}\cdot(\mathbf{R}+\tau_p)}\ , \tag{A3}$$

where $Y_L(\mathbf{r})$ is a spherical harmonic, and $\mathbf{r}_p=\mathbf{r}-\tau_p$ is the position in unit cell measured from the pth lattice site. The plane-wave basis functions are defined as

$$|\,\mathbf{k}+\mathbf{G}\,\rangle=\frac{1}{(N\Omega_0)^{1/2}}e^{i(\mathbf{k}+\mathbf{G})\cdot\mathbf{r}}\ , \tag{A4}$$

where N is the number of unit cells in the crystal and Ω_0 is the unit-cell volume.

The overlap matrix S is given by

$$\begin{aligned}&S_{\mathbf{k}+\mathbf{G},\mathbf{k}+\mathbf{G}'}=\delta_{\mathbf{G},\mathbf{G}'}\ ,\\ &S_{\mathbf{k}+\mathbf{G},pL}=F_{pl}(G)f_{pl}(\,|\,\mathbf{k}+\mathbf{G}\,|\,)Y_L(\mathbf{k}+\mathbf{G})\ ,\\ &S_{pL,p'L'}=\delta_{p,p'}\delta_{L,L'}\ ,\end{aligned} \tag{A5}$$

where the structure factor is

$$F_{pl}(\mathbf{G})=\frac{4\pi i^{-l}}{(\Omega_0)^{1/2}}e^{-iG\cdot\tau_p}$$

and

$$f_{pl}(\,|\,\mathbf{k}+\mathbf{G}\,|\,)=\int j_l(\,|\,\mathbf{k}+\mathbf{G}\,|\,r)f_{p,l}(r)r^2dr\ .$$

The Hamiltonian matrix elements are

$$H_{\mathbf{k}+\mathbf{G},\mathbf{k}+\mathbf{G}'} = |\mathbf{k}+\mathbf{G}|^2\delta_{\mathbf{G},\mathbf{G}'} + U^{\rm nl}_{\mathbf{k}+\mathbf{G},\mathbf{k}+\mathbf{G}'} + V^{LH\rm xc}_{\mathbf{G}-\mathbf{G}'} ,$$

$$H_{\mathbf{k}+\mathbf{G},pL} = T_{\mathbf{k}+\mathbf{G},pL} + U^{\rm nl}_{\mathbf{k}+\mathbf{G},pL} + V^{LH\rm xc}_{\mathbf{k}+\mathbf{G},pL}[\rho] ,$$

$$H_{pL,p'L'} = \delta_{p,p'}\delta_{L,L'}[T_{pL,pL} + U^{\rm nl}_{pL,pL}] + V^{LH\rm xc}_{pL,p'L'}[\rho] .$$

As indicated, the kinetic energy and the nonlocal part of the pseudopotential are completely diagonal within the local function subspace. Since the kinetic energy and nonlocal part of the pseudopotential are independent of the charge density, matrix elements involving these operators are only evaluated in the first iteration of the self-consistent procedure and stored for use in later iterations.

A variety of methods are used to evaluate the matrix elements. Our discussion begins with the simplest terms and proceeds to the more complicated terms. The only nontrivial part of the overlap matrix S is that between plane waves and localized functions. As indicated in Eq. (A5), these factor into an angular part that can be evaluated analytically and a part that depends on the magnitude of the reciprocal-space vector $\mathbf{k}+\mathbf{G}$. This latter part is evaluated on a numerical mesh and is interpolated to find the value at $|\mathbf{k}+\mathbf{G}|$.

The plane-wave—plane-wave matrix elements of the kinetic energy are diagonal and computed as needed. The kinetic energy part of the plane-wave—local matrix elements are found from the plane-wave—local overlap integrals using the relation

$$T_{\mathbf{k}+\mathbf{G},pL} = |\mathbf{k}+\mathbf{G}|^2 S_{\mathbf{k}+\mathbf{G},pL} .$$

The special construction of the LCAO basis functions ensures that the local-local kinetic energy matrix elements are rigorously diagonal in lattice site and angular momentum, and are independent of the wave vector. This results in a significant computational savings compared to earlier implementations of this technique.[17] We evaluate these elements using a momentum space integral involving the Fourier transform of the atomic functions:

$$T_{pL,pL} = \langle \phi_{pL} | \nabla^2 | \phi_{pL} \rangle = \frac{2}{\pi}\int_0^{q_{\max}} |J_{pl}(q)|^2 q^4 dq , \tag{A6}$$

where

$$J_{pl}(q) = \int_0^\infty f_{pl}(r) j_l(qr) r^2 dr .$$

This procedure is generally considered to be more accurate numerically than a differencing scheme to evaluate derivatives, but does require that we compute the Fourier transform of our optimized basis functions. In principle, it is not possible to localized a function in real space and Fourier space. This, together with discrete nature of our basis functions and the quartic term in the sum leads to a slight numerical instability as $q_{\max}$ is increased. The value of the kinetic energy we use is taken from the average of values in the horizontal region of the curve between 400 to 600 a.u. (see Fig. 9).

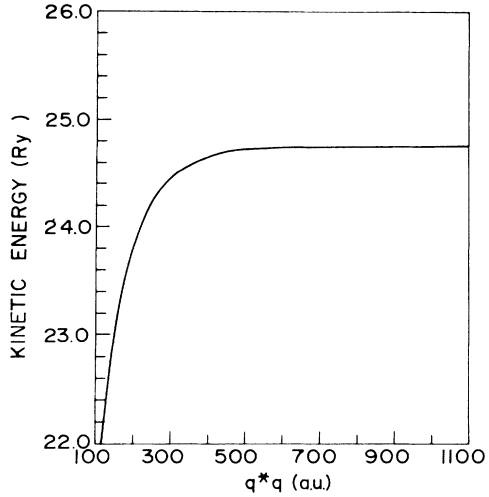

FIG. 9. Convergence of the diagonal kinetic energy term for the "optimized" local function with cutoff of the $\mathbf{q}$ space integral in Eq. (A6).

The (fully diagonal) local-local matrix elements of $U^{\rm nl}$ are evaluated directly by summation on a numerical real-space radial mesh:

$$U^{\rm nl}_{pL,pL} = \langle \phi_{pL} | U^{\rm nl} | \phi_{pL} \rangle = \int_0^\infty f^2_{p,l}(r) U^{\rm nl}_{p,l}(r) r^2 dr .$$

This term (and the corresponding kinetic energy term) are independent of crystal structure.

The plane-wave—local matrix elements of the nonlocal potential have the form

$$U^{\rm nl}_{\mathbf{k}+\mathbf{G},pL} = F_{pl}(\mathbf{G}) Y_L(\mathbf{k}+\mathbf{G}) \int_0^\infty j_l(|\mathbf{k}+\mathbf{G}| r) U^{\rm nl}_{p,l}(r) \times f_{p,l}(r) r^2 dr .$$

The factor before the integral is evaluated as needed, while the integral is found with a look-up procedure on a precomputed table of values.

The matrix elements of the nonlocal pseudopotential within the plane-wave subspace are evaluated using the expression

$$U^{\rm nl}_{\mathbf{k}+\mathbf{G},\mathbf{k}+\mathbf{G}'} = F_{pl}(\mathbf{G}) F^*_{pl}(\mathbf{G}') \sum_l (2l+1) P_l(\Theta_{\mathbf{k}+\mathbf{G},\mathbf{k}+\mathbf{G}'}) \int U^{\rm nl}_{pl}(r) j_l(|\mathbf{k}+\mathbf{G}| r) j_l(|\mathbf{k}+\mathbf{G}'| r) r^2 dr .$$

The matrix elements of the combined local potentials, $V^{LH\rm xc}$, is evaluated as follows. The plane-wave—plane-wave part is trivial because the potential is represented on a reciprocal-space mesh. (The computation of this potential from the eigenvectors is discussed in Appendix C.) The plane-wave—local matrix elements are evaluated in one step by a "partial" fast Fourier transform (FFT) of the quantity

$$P_{pL}(\mathbf{r}) = V^{LH\rm xc}(\mathbf{r}) \phi_{pL}(\mathbf{r}) .$$

The term "partial FFT" refers to a technique we developed for efficiently finding a small number of

Fourier coefficients of a function known on a dense real-space mesh. The technique is described in Appendix B.

The local-local matrix elements are more involved. In previous work, these terms were evaluated by transforming the potential and local-basis functions to a real-space mesh with the FFT and summing in real space. Because of the difficulty in retaining high precision with the large FFT that would be required for the localized functions in the present case, we elected to use an approach requiring only one-dimensional numerical integrations. By expanding the exponential term in the Fourier transform of $V^{LH\mathrm{xc}}$, we arrive at the following form:

$$V^{LH\mathrm{xc}}_{pL,p'L'}=\sum_{\mathbf{G}} V^{LH\mathrm{xc}}(\mathbf{G})\int e^{i\mathbf{G}\cdot\mathbf{r}}\phi^{*}_{pL}(\mathbf{r})\phi_{p'L'}(\mathbf{r})d\mathbf{r}$$

$$=4\pi\sum_{\mathbf{G}} V^{LH\mathrm{xc}}(\mathbf{G})\left[e^{i\mathbf{G}\cdot\tau_p}\sum_{L''} i^{-l''}Y_{L''}(\hat{\mathbf{G}})C(L,L',L'')K_{l,l',l''}(G)\right], \tag{A7}$$

where

$$C(L,L',L'')=\int Y^{*}_{L}(\hat{\mathbf{r}})Y_{L'}(\hat{\mathbf{r}})Y^{*}_{L''}(\hat{\mathbf{r}})d\hat{\mathbf{r}}$$

are Gaunt coefficients that can be evaluated with a look-up scheme (since only a few terms are required) and

$$K_{l,l',l''}=\int_0^{\infty} f_{pl}(r)f_{p'l'}(r)j_{l''}(Gr)r^2dr\ .$$

The term within large parentheses in Eq. (A7) can be evaluated once and stored, and K can be evaluated with a look-up scheme from a precomputed table of values.

APPENDIX B: PARTIAL FFT

In this appendix the technical details of the "partial" fast Fourier transform (FFT) procedure is discussed. The procedure is designed to solve the problem of efficiently calculating a limited number of Fourier components of a function known on a fine (dense) mesh in real space. The functions we are concerned with have the periodicity of the crystal lattice. Accordingly, we assume that they are known on a set of points in real space within the Wigner-Seitz cell; the problem is to find their long-wavelength Fourier coefficients without calculating *all* the coefficients and then discarding the unwanted ones.

Let $\{\mathbf{r}_i\}$ denote the dense real-space mesh and let $f(\mathbf{r}_i)$ be a function known on this mesh. The set $\{\mathbf{r}_i\}$, of size N, is conjugate by construction to a large set of reciprocal-lattice vectors $\{\mathbf{G}_j\}$. Let $\{\mathbf{g}_j\}$ be the subset of $\{\mathbf{G}_j\}$ containing the limited number n of reciprocal-lattice vectors for which we seek the transform of $f(\mathbf{r}_i)$. We choose $\{\mathbf{g}_j\}$ (by including a few unwanted reciprocal-lattice vectors if necessary) so that periodic extension of the volume containing it generates the large set $\{\mathbf{G}_j\}$.

By construction $\{\mathbf{g}_j\}$ is conjugate to a course real-space mesh $\{\mathbf{R}_k\}$ containing n vectors within the Wigner-Seitz cell. Every vector in $\{\mathbf{r}_i\}$ may be written as the sum of an element of $\{\mathbf{R}_k\}$ and a vector τ contained in a cell (a reduced Wigner-Seitz cell) centered on each $\mathbf{R}_k$:

$$\mathbf{r}_i=\mathbf{R}_k+\tau_m \tag{B1}$$

or schematically

$$\{\mathbf{r}_i\}=\{\mathbf{R}_k\}\times\{\tau_m\}\ .$$

By construction, there are N/n vectors in $\{\tau_m\}$.

Computational efficiency dictates that the small set of reciprocal-lattice vectors $\{\mathbf{g}_j\}$ be just large enough to describe the highest-frequency components of the quantity of interest. To take optimal advantage of the FFT algorithm, however, the size of this set n should be a highly composite number and we may wish to enlarge the cell slightly to achieve this. For example, an initial choice of a $\{\mathbf{G}_j\}$ containing $(11)^3$ points could be improved by increasing to $(12)^3=(2)^6(3)^3$ points.

We are interested in the evaluating quantities such as

$$F(\mathbf{g}_j)=\sum_{i=0}^{N-1} e^{-i\mathbf{g}_j\cdot\mathbf{r}_i}f(\mathbf{r}_i)\ . \tag{B2}$$

With use of (B1) this may be rewritten as

$$F(\mathbf{g}_j)=\sum_{k=0}^{n-1}\sum_{m=0}^{N/n-1} e^{-i\mathbf{g}_j\cdot(\tau_m+\mathbf{R}_k)}f(\tau_m+\mathbf{R}_k)$$

$$=\sum_{m=0}^{N/n-1} e^{-i\mathbf{g}_j\cdot\tau_m}\left[\sum_{k=0}^{n-1} e^{-i\mathbf{g}_j\cdot\mathbf{R}_k}h_m(\mathbf{R}_k)\right], \tag{B3}$$

where we have written

$$h_m(\mathbf{r}_k)=f(\mathbf{R}_k+\tau_m) \tag{B4}$$

to emphasize that the term within large parentheses can be evaluated with an FFT.

To compare the performance of this reduced FFT to an FFT over the entire set $\{\mathbf{G}_i\}$, we estimate and compare the number of operations required in the two procedures. The term "operation" denotes a complex multiplication and a complex addition, and for convenience, we assume a uniradix transform. From Eq. (B2), we require N/n-independent transforms (which can be evaluated in parallel), each of which requires $n\ln n$ operations. For each $\mathbf{g}_j$, N/n explicit operations are also required. Thus the total number of operations is $(N/n)n(\ln n+1)=N(\ln n+1)$, which should be compared to $N\ln N$ operations if the FFT were performed over the large set $\{\mathbf{r}_i\}$. For the present case, a 50% savings in the number of operations is achieved on average.

APPENDIX C: CHARGE DENSITY CALCULATION

We have to calculate the charge density and the corresponding new output potential to iterate our potential to self-consistency. We need $\rho(\mathbf{G})$ t evaluate $V^H(\mathbf{G})=4\pi e^2\rho(\mathbf{G})/G^2$ and $\rho(\mathbf{r})$ to evaluate $V^{\mathrm{xc}}(\rho)$. Owing to the factor of $1/G^2$, the higher $\mathbf{G}$ components of $V^H(\mathbf{G})$ converge more quickly than $\rho(\mathbf{G})$.

In order to calculate $\rho(\mathbf{r})$ accurately from $\rho(\mathbf{G})$ by using the FFT, we need to employ very high $\mathbf{G}$-vector components of $\rho(\mathbf{G})$, because $\rho(\mathbf{r})$ has rapid spatial variations near the nuclei. We have found this to be an impractical procedure and have developed a new method to evaluate $\rho(\mathbf{r})$ directly on the finite mesh points in real space. Even with the new method the number of mesh points might well be a problem [due to the sharpness of $\rho(\mathbf{r})$], but the final quantity that we need is the exchange-correlation energy functional, which is much smoother than $\rho(\mathbf{r})$. While the method is a bit complicated, it is more efficient and accurate than the usual FFT method. In addition, the fully symmetrized $\rho(\mathbf{G})$ is obtained as a side benefit with little additional effort.

As discussed in the text, the eigenfunctions are expanded as a sum of plane wave and LCAO's constructed from localized nonoverlapping functions,

$$\Psi_{n\mathbf{k}}(\mathbf{r})=\sum_{G}\alpha_{n\mathbf{k}}(\mathbf{G})\,|\,\mathbf{k}+\mathbf{G}\rangle+\sum_{p,L}d_{pL}(n\mathbf{k})\phi_{pL}(\mathbf{k};\mathbf{r})\ . \tag{C1}$$

The charge density in the crystal is

$$\rho(\mathbf{r})=\sum_{n,\mathbf{k}}2\Theta(\epsilon_f-\epsilon_{n\mathbf{k}})\,|\,\Psi_{n\mathbf{k}}(\mathbf{r})\,|^2\ ,$$

where $\Theta(\epsilon)$ is a step function which is zero for $\epsilon<0$ and 1 for $\epsilon>0$. When combined with the normalization factor $1/N$, the sum over $\mathbf{k}$ becomes an average over the whole Brillouin zone.

Rather than attempting to compute the energy band at a large number of wave vectors, we use a Gaussian weighting scheme which makes it possible to represent the average behavior near the Fermi energy with a relatively coarse mesh in the BZ (in practice, 30 to 35 points in IBZ are used). The sum over the full BZ is equivalent to a sum over the IBZ:

$$\frac{1}{N_{\mathbf{k}}}\sum_{\mathbf{k}}^{\mathrm{BZ}}(\cdots)\rightarrow\frac{1}{N_{\mathrm{op}}}\sum_{R_{\mathrm{op}}}\sum_{\mathbf{k}}^{\mathrm{IBZ}}w(\mathbf{k})(\cdots)\ ,$$

where R_{op} represents a point group operator of the system and $w(\mathbf{k})$ is a geometric weighting factor for each $\mathbf{k}$ in the IBZ. We replace the occupancy factor $2\Theta(\epsilon_f-\epsilon_{n\mathbf{k}})$ with $W_{n\mathbf{k}}$, a new occupancy number determined by a Gaussian weighting scheme. Then,

$$\rho(\mathbf{r})=\frac{1}{N_{\mathrm{op}}}\sum_{R_{\mathrm{op}}}R_{\mathrm{op}}\left[\sum_{n,k}{}'w(\mathbf{k})W_{n\mathbf{k}}\rho_{n\mathbf{k}}(\mathbf{r})\right]\ , \tag{C2}$$

where $\rho_{n\mathbf{k}}$ is the square modulus of (C1), and here and below the prime on the $n\mathbf{k}$ summation indicates a sum over the irreducible $\frac{1}{48}$th of the Brillouin zone. Substitution of the explicit form of the wave function yields

$$\rho(\mathbf{r})=\rho_{\mathrm{pw}}(\mathbf{r})+\rho_{\mathrm{loc}}(\mathbf{r})+\rho_{\mathrm{mix}}(\mathbf{r})\ , \tag{C3}$$

corresponding to the plane-wave—plane-wave, local-local, and plane-wave—local terms in the sum of the squares of the occupied eigenfunctions. We discuss these in turn below.

1. Plane-wave part of the charge density in r space

Our aim is to express the part of the charge density arising from a complete Brillouin zone sum of the square of the plane-wave part of the eigenfunctions as a weighted sum over the irreducible fraction of the zone. Using (C1) and (C2) we find

$$\rho_{\mathrm{pw}}(\mathbf{r})=\frac{1}{N_{\mathrm{op}}}\sum_{R_{\mathrm{op}}}R_{\mathrm{op}}\sum_{n,\mathbf{k}}{}'w(\mathbf{k})W_{n\mathbf{k}}\frac{1}{\Omega_0}\times\sum_{\mathbf{G},\mathbf{G}'}\alpha_{n\mathbf{k}}(\mathbf{G})\alpha^*_{n\mathbf{k}}(\mathbf{G}')e^{i(\mathbf{G}-\mathbf{G}')\cdot\mathbf{r}}$$

which can be rewritten in the form

$$\rho_{\mathrm{pw}}(\mathbf{r})=\frac{1}{N_{\mathrm{op}}}\sum_{R_{\mathrm{op}}}R_{\mathrm{op}}\sum_{\mathbf{G},\mathbf{G}'}A_{\mathbf{G}\mathbf{G}'}e^{i(\mathbf{G}-\mathbf{G}')\cdot\mathbf{r}}\ ,$$

where

$$A_{\mathbf{G}\mathbf{G}'}=\frac{1}{\Omega_0}\sum_{n,\mathbf{k}}{}'w(\mathbf{k})W_{n\mathbf{k}}\alpha_{n\mathbf{k}}(\mathbf{G})\alpha^*_{n\mathbf{k}}(\mathbf{G}')\ .$$

The quantity

$$P(\mathbf{r}_i)=\sum_{\mathbf{G},\mathbf{G}'}A_{\mathbf{G},\mathbf{G}'}e^{i(\mathbf{G}-\mathbf{G}')\cdot\mathbf{r}_i}\ ,$$

where $\{\mathbf{r}_i\}$ is the real-space mesh conjugate to the reciprocal-lattice vectors used to expand the plane-wave part of the eigenfunctions, is a simple Fourier transform which can be done easily by an FFT of small size. The vectors $\mathbf{r}_i$ have the same symmetry as the G's because these are defined on a FFT mesh. Therefore,

$$\rho_{\mathrm{pw}}(\mathbf{r}_i)=\frac{1}{N_{\mathrm{op}}}\sum_{R_{\mathrm{op}}}R_{\mathrm{op}}P(\mathbf{r}_i)=\frac{1}{N_{\mathrm{op}}}\sum_{R_{\mathrm{op}}}P(R_{\mathrm{op}}\mathbf{r}_i)\ .$$

Because the real-space mesh in the FFT has the lattice symmetry, $R_{\mathrm{op}}\mathbf{r}_i$ is another mesh point in the Wigner-Seitz unit cell. Therefore, the plane-wave part of charge density is easily calculated and symmetrized on a coarse spatial mesh.

2. Localized part of charge density in r space

The localized functions employed here are strictly nonoverlapping. Accordingly, we may without approximation compute this part of the charge density in the central unit cell at $\mathbf{R}=0$. The result is

$$\begin{aligned}\rho_{\mathrm{loc}}(\mathbf{r})&=\frac{1}{N_{\mathrm{op}}}\sum_{R_{\mathrm{op}}}R_{\mathrm{op}}\sum_{n\mathbf{k}}{}'w(\mathbf{k})W_{n\mathbf{k}}\sum_{p,L,L'}d_{pL}(n\mathbf{k})d_{pL'}(n\mathbf{k})\phi_{pL}(\mathbf{r}_p)\phi^*_{pL'}(\mathbf{r}_p)\\&=\frac{1}{N_{\mathrm{op}}}\sum_{R_{\mathrm{op}}}R_{\mathrm{op}}\sum_{p,L,L'}\left[\sum_{n,\mathbf{k}}{}'w(\mathbf{k})W_{n\mathbf{k}}d_{pL}(n\mathbf{k})d_{pL'}(n\mathbf{k})\right]\phi_{pL}(\mathbf{r}_p)\phi_{pL'}(\mathbf{r}_p)^*\\&=\frac{1}{N_{\mathrm{op}}}\sum_{R_{\mathrm{op}}}R_{\mathrm{op}}\sum_{p,L,L'}D_{pLL'}\phi_{pL}(\mathbf{r}_p)\phi^*_{pL'}(\mathbf{r}_p)\ ,\end{aligned} \tag{C4}$$

where

$$D_{pLL'}=\sum_{n,\mathbf{k}}{}' w(\mathbf{k})W_{n\mathbf{k}}d_{pL}(n\mathbf{k})d_{pL'}(n\mathbf{k}) .$$

The transformation properties of the localized functions are known and may be used to simplify this expression. Since atom site p transforms onto itself under point-group rotations (given that the unit cell contains only one atom of a given species) the rotated functions in (C4) are linear combinations of the localized functions on the same lattice site. Temporarily suppressing the indices p and l,

$$R_{\rm op}\phi_m=\sum_{m'}A_{m,m'}(R_{\rm op})\phi_{m'} ,$$

where m is the magnetic quantum number and $A_{m,m'}$ is the rotation matrix for angular momentum l corresponding to $R_{\rm op}$. Since the result of the group operation is to replace a particular localized function by a linear combination of functions on the same lattice site, Eq. (C4) is equivalent to the simpler expression

$$\rho_{\rm loc}(\mathbf{r})=\sum_{p,L,L'}\tilde{D}_{pLL'}\phi_{pL}(\mathbf{r}_p)\phi^*_{pL'}(\mathbf{r}_p) , \tag{C5}$$

where the "symmetrized" coefficients $\tilde{D}$ are themselves given by

$$\tilde{D}_{pLL'}=\frac{1}{N_{\rm op}}\sum_{R_{\rm op}}\sum_{m_1}\sum_{m_2}A_{m,m_1}(R_{\rm op})D_{pL_1L_2}A_{m',m_2}(R_{\rm op}) .$$

The quantity $\tilde{D}_{pLL'}$ is just a coefficient and $\phi_{pL}(\mathbf{r}_p)$ may be read from a premade atomic data file that contains wave-function values on a sufficiently fine mesh. Thus, the accumulation and symmetrization of charge density information related to the local-local part of the square of the eigenfunctions involves only the small number of quantities $\tilde{D}_{pLL'}$ which need be combined with the large number of ϕ_{pL} values as the last step of the calculation.

3. Mixed part of charge density in r space

The third term in the charge density is the cross term between the plane wave and localized-function expansion of the eigenfunctions. We define

$$u_{n\mathbf{k}}(\mathbf{r})=\frac{1}{(\Omega_0)^{1/2}}\sum_{\mathbf{G}}\alpha_{n\mathbf{k}}(\mathbf{G})e^{i\mathbf{G}\cdot\mathbf{r}}$$

to be the periodic part of the plane-wave component of the eigenfunction. Then in the central cell the mixed part of the charge density may be written in the form

$$\rho_{\rm mix}(\mathbf{r})=\frac{1}{N_{\rm op}}\sum_{R_{\rm op}}R_{\rm op}\left[\sum_{p,L}\left[\sum_{n,\mathbf{k}}{}' w(\mathbf{k})W_{n\mathbf{k}}e^{-i\mathbf{k}\cdot(\mathbf{r}_p)}u^*_{n\mathbf{k}}(\mathbf{r})d_{pL}(n\mathbf{k})\right]\phi_{pL}(\mathbf{r}_p)+\text{c.c.}\right] .$$

We define

$$B_{pL}(\mathbf{r})=\sum_{n,\mathbf{k}}{}' w(\mathbf{k})W_{n\mathbf{k}}e^{-i\mathbf{k}\cdot(\mathbf{r}_p)}u_{n\mathbf{k}}(\mathbf{r})d^{pL}(n\mathbf{k})$$

and accumulate this quantity on the coarse r mesh. Then, bringing the rotation operators inside the functions yields

$$\rho_{\rm mix}(\mathbf{r})=\sum_{p,L}\frac{1}{N_{\rm op}}\sum_{R_{\rm op}}B_{pL}(R_{\rm op}\mathbf{r})\phi_{pL}[R_{\rm op}(\mathbf{r}_p)] .$$

Using

$$\phi_{pL}[R_{\rm op}(\mathbf{r}_p)]=\sum_{L'}A_{LL'}(R_{\rm op})\phi_{pL'}(\mathbf{r}_p) ,$$

we rewrite this in the form

$$\begin{aligned}\rho_{\rm mix}(\mathbf{r})&=\sum_p\left[\frac{1}{N_{\rm op}}\sum_{R_{\rm op}}\sum_{L,L'}B_{pL}(R_{\rm op}\mathbf{r})A_{LL'}(R_{\rm op})Y_{L'}(\mathbf{r}_p)\right.\\&\qquad\left.+\text{c.c.}\right]f_p(|\mathbf{r}_p|)\\&=\sum_p\tilde{B}_p(\mathbf{r})f_p(|\mathbf{r}_p|) .\end{aligned}\tag{C6}$$

The quantity $\tilde{B}_p$ involves only the plane-wave part of the eigenfunctions. Accordingly, we accumulate it on the course r mesh and interpolate it, using the FFT procedure described earlier, onto the fine $\mathbf{r}$ mesh at the last step of the calculation.

Now we turn to the calculation of the density in $\mathbf{G}$ space. The most direct method is to use an FFT on the real-space function because we have already obtained the information of $\rho(\mathbf{r})$ on the FFT mesh. Although this is practical for $V_{\rm xc}(\mathbf{r})$ due to the smoothness of the potential, the uniformly spaced $\mathbf{r}$ mesh is still not dense enough to represent $\rho(\mathbf{r})$. For example, in our calculations, the exchange and correlation potential $v_{\rm xc}$ is typically well described by a set of $12K$ reciprocal-lattice vectors; the full charge density would require of order $30K$ $\mathbf{G}$ vectors. Analytic treatments of the localized part of the $\Psi_{n\mathbf{k}}$ will provide the most efficient approach to the problem.

The decomposition (C3) in real space implies an analogous decomposition in reciprocal space. We write

$$\begin{aligned}\rho(\mathbf{G})&=\frac{1}{\Omega_0}\int_{\Omega_0}e^{-i\mathbf{G}\cdot\mathbf{r}}\rho(\mathbf{r})d\mathbf{r}\\&=\rho_{\rm pw}(\mathbf{G})+\rho_{\rm loc}(\mathbf{G})+\rho_{\rm mix}(\mathbf{G}) .\end{aligned}$$

We will evaluate each contribution in turn.

4. Plane-wave part of charge density in G space

The plane-wave part of the charge density was evaluated on the course mesh in reciprocal space. However, this function is intrinsically smooth because it was constructed from the lower $\mathbf{G}$ vector components of eigenfunction. Therefore, the $\rho_{\rm pw}(\mathbf{G})$ can be obtained by FFT on the course mesh without any loss of accuracy.

5. Localized part of charge density in G space

Fourier transformation of Eq. (C5) yields

$$\rho_{\rm loc}(\mathbf{G})=\frac{1}{\Omega_0}\int_{\Omega_0} e^{-i\mathbf{G}\cdot\mathbf{r}}\sum_{p,L,L'}\widetilde{D}_{pLL'}\phi_{pL}(\mathbf{r}_p)\phi^*_{pL'}(\mathbf{r}_p)d\mathbf{r}\ .$$

Changing the integration variable leads to

$$\rho_{\rm loc}(\mathbf{G})=\frac{1}{\Omega_0}\sum_{p,L,L'}\widetilde{D}_{pLL'}e^{-i\mathbf{G}\cdot\tau_p}\times\int_{\Omega_0} e^{-i\mathbf{G}\cdot\mathbf{r}}\phi_{pL}(\mathbf{r})\phi^*_{pL'}(\mathbf{r})d\mathbf{r}\ . \qquad \text{(C7)}$$

We expand the plane wave and the atomic wave function

$$e^{-i\mathbf{G}\cdot\mathbf{r}}=\sum_{l,m}4\pi(-i)^l Y^*_{lm}(\mathbf{G})Y_{lm}(\mathbf{r})j_l(Gr)\ ,$$

$$\phi_{pL}(\mathbf{r})=f_p(r)Y_L(\mathbf{r})\ ,$$

which allows us to separate the integral in (C7) into radial and angular parts. The radial part is a Bessel transform which can be done very accurately in a dense one-dimensional mesh. The angular integration of the product of three spherical harmonic functions yields the Gaunt coefficients $C(L,L',L'')$. Since $\rho(G)$ has the symmetry of the crystal, selection rules limit the ensuing sum to only a few nonvanishing coefficients which are obtained analytically. The result is

$$\rho_{\rm loc}(\mathbf{G})=\frac{4\pi}{\Omega_0}\sum_{p,L,L'}\widetilde{D}_{pLL'}e^{-i\mathbf{G}\cdot\tau_p}\sum_{L''}(-i)^{l''}C(L,L',L'')Y_{L''}(\mathbf{G})\int f_p(r)^2 j_{l''}(r)r^2dr\ .$$

For a charge density constructed from localized functions with d symmetry, the $l=0$, 2, and 4 Bessel transforms are required in this expression. We should also note that $\rho_{\rm loc}(\mathbf{G})$ need only be accumulated on a set of representative $\mathbf{G}$ vectors which provide the expansion in each star of $\mathbf{G}$.

6. Mixed part of charge density in G space

We need to evaluate the Fourier transform of (C6):

$$\rho_{\rm mix}(\mathbf{G})=\frac{1}{\Omega_0}\int_{\Omega_0} e^{-i\mathbf{G}\cdot\mathbf{r}}\sum_p \widetilde{B}_p(\mathbf{r})f_p(\,|\,\mathbf{r}_p\,|\,)\ .$$

Since $\widetilde{B}_p(\mathbf{r})$ is a smooth function, we expand it in Fourier series

$$\widetilde{B}_p(\mathbf{r})=\sum_{\mathbf{G}'}e^{i\mathbf{G}'\cdot\mathbf{r}}\widetilde{B}_p(\mathbf{G}')=\sum_{\mathbf{G}'}e^{i\mathbf{G}'\cdot\tau_p}e^{i\mathbf{G}'\cdot(\mathbf{r}-\tau_p)}\widetilde{B}_p(\mathbf{G}')$$

which leads to

$$\rho_{\rm mix}(\mathbf{G})=\frac{1}{\Omega_0}\sum_p\sum_{\mathbf{G}'}e^{-i(\mathbf{G}-\mathbf{G}')\cdot\tau_p}\widetilde{B}_p(\mathbf{G}')\times\int_{\Omega_0} e^{-i(\mathbf{G}-\mathbf{G}')\cdot\mathbf{r}}f_p(r)d\mathbf{r}\ . \qquad \text{(C8)}$$

Since $f(r)$ is spherically symmetric, this reduces to a zeroth-order Bessel transform of the radial function. Although a direct evaluation of (C8) would require $\{N_g\times N_g\}$ operations where N_g is the number of plane waves required to span ϕ_p, there are two features in the structure of (C8) which allow a considerably reduced calculation. First, the quantity $\rho_{\rm mix}(\mathbf{G})$ has the point-group symmetry of the crystal by construction, and therefore only needs to be evaluated on a set of representative $\mathbf{G}$'s. Second, the intermediate sum over $\mathbf{G}'$ is self-limiting because of the smooth form of $\widetilde{B}$. The number of operations involved in evaluating (C8) is so small that the calculation runs relatively quickly.

Once $\rho(\mathbf{G})$ has been accumulated on a set of representative $\mathbf{G}$'s the Hartree potential is combined with the reciprocal-lattice representation of the exchange and correlation potential as described in Appendix A, and the resulting screening potential is returned to be included as an input potential in the SCF cycle in the usual way.

[1] M. L. Cohen, Phys. Rep. **110**, 293 (1984).
[2] W. Kohn and L. J. Sham, Phys. Rev. **140**, A1133 (1965).
[3] D. M. Ceperley and B. J. Alder, Phys. Rev. Lett. **45**, 566 (1980).
[4] J. P. Perdew and A. Zunger, Phys. Rev. B **23**, 5048 (1981).
[5] G. B. Bachelet, D. R. Hamann, and M. Schlüter, Phys. Rev. B **26**, 4199 (1982); **29**, 2309(E) (1984); G. Kerker, J. Phys. C **13**, L189 (1980); J. D. Joannopoulos, Th. Starkloff, and M. Kastner, Phys. Rev. Lett. **38**, 660 (1977).
[6] M. T. Yin and M. L. Cohen, Phys. Rev. B **26**, 5668 (1982).
[7] K. J. Chang and M. L. Cohen, Phys. Rev. B **31**, 7819 (1985).
[8] K. M. Rabe and J. Joannopoulos, Phys. Rev. B **32**, 2302 (1985).
[9] J. R. Chelikowsky and S. G. Louie, Phys. Rev. B **29**, 3470 (1984).
[10] D. Vanderbilt and S. G. Louie, Phys. Rev. B **30**, 6118 (1984).
[11] J. A. Appelbaum and D. R. Hamann, Bul. Am. Phys. Soc. **23**, 364 (1978).
[12] S. G. Louie, K. M. Ho, and M. L. Cohen, Phys. Rev. B **19**, 1774 (1979).
[13] C.-L. Fu and K.-M. Ho, Phys. Rev. B **28**, 5480 (1983); and private communication.
[14] A. Zunger and M. L. Cohen, Phys. Rev. B **19**, 568 (1979).
[15] C. Y. Fong and M. L. Cohen, Phys. Rev. Lett. **24**, 306 (1970).
[16] C. Y. Fong, J. P. Walter, and M. L. Cohen, Phys. Rev. B **11**, 2759 (1975).
[17] N. A. W. Holzwarth, S. G. Louie, and S. Rabii, Phys. Rev. B

30, 2219 (1984).
[18]P. Bendt and A. Zunger, Phys. Rev. B **26**, 3114 (1982).
[19]V. L. Moruzzi, J. F. Janak, and A. R. Williams, *Calculated Electronic Properties of Metals* (Pergamon, New York, 1978).
[20]M. R. Norman, Phys. Rev. B **29**, 2956 (1984).
[21]J. A. Knapp, F. J. Himpsels, and D. E. Eastman, Phys. Rev. B **19**, 4952 (1979).
[22]J. F. Janak, A. R. Williams, and V. L. Moruzzi, Phys. Rev. B **11**, 1522 (1975).
[23]J. Ihm, A. Zunger, and M. L. Cohen, J. Phys. C **12**, 4401 (1979).
[24]A. R. Williams, J. Kübler, and C. D. Gelatt, Jr., Phys. Rev. B **19**, 6094 (1979).
[25]The lattice constant was obtained from *American Institute of Physics Handbook,* 3rd ed. (McGraw-Hill, New York, 1972), Table 9d-3. The cohesive energy was from R. Hultgren, R. L. Orr, and K. K. Kelley, *Selected Values of Thermodynamic Properties of Metals and Alloys* (Wiley, New York, 1965). The bulk modulus was from *Physical Acoustics,* edited by W. P. Mason (Academic, New York, 1965), Vol. III-B, Appendix I.